Spatial correlation functions of paracrystals with radial symmetry

Guan-Rong Huang,[1,*] Yangyang Wang,[2] Changwoo Do,[1] and Wei-Ren Chen[1,†]
[1]*Neutron Scattering Division, Oak Ridge National Laboratory, Oak Ridge, Tennessee 37831, USA*
[2]*Center for Nanophase Materials Sciences, Oak Ridge National Laboratory, Oak Ridge, Tennessee 37831, USA*

(Received 26 April 2020; accepted 19 August 2020; published 8 September 2020)

We develop a phenomenological model to describe the structure of radially symmetric paracrystals whose long-range order are destroyed by propagation of particle fluctuations. General expressions are derived for the spatial correlation functions in one-, two-, and three-dimensional spaces. And the spatial correlation in paracrystals in reciprocal space is further discussed and clarified. The developed method can be used to quantitatively analyze the microstructure of paracrystalline materials in both real and reciprocal spaces via scattering experiments and computer simulations.

DOI: 10.1103/PhysRevE.102.032110

I. PHENOMENOLOGICAL MODEL OF PARACRYSTALS WITH RADIAL SYMMETRY

In this work we consider the two-point correlation functions of paracrystals with radial symmetry, first discussed in detail by R. Hosemann [1–3]. Although the previous studies of paracrystals have enjoyed some success by describing the properties of metal, protein, glass, and soft materials with Cartesian symmetry [1,2,4–15], the theory of paracrystals with radial symmetry remains to be further developed for potential applications in various amorphous materials. This provides the main motivation for this work. A key concept in constructing a paracrystal model is the propagation and accumulation of particle fluctuations. Along the radial direction throughout the lattice, the long-range order is destroyed by the accumulated fluctuations. Following the method of Hosemann and Guinier, we can express the radial distribution function $g(r)$ as the sum of probability distributions $h_n(r)$ associated with different shells with mean nL and variance $n\sigma^2$,

$$g(r) = \sum_{n=1}^{\infty} h_n(r). \tag{1}$$

Based on the properties of paracrystals in different shells, one can construct $h_2(r), h_3(r) \ldots h_n(r)$ according to the following procedure:

$$\begin{aligned} h_2(r) &= \frac{\int dr' h_1(r') h_1(r-r')}{\int dr' h_1(r')}, \\ h_n(r) &= \frac{\int dr' h_{n-1}(r') h_1(r-r')}{\int dr' h_1(r')}, \end{aligned} \tag{2}$$

which can be recognized as one-dimensional convolution of the radial variable. It can be shown that $h_n(r)$ in Eq. (2) satisfies the characteristics of paracrystals in the radial direction

$$r_n = \int dr r h_n(r) = nL, \sigma_n^2 = \int dr (r-r_n)^2 h_n(r) = n\sigma^2, \tag{3}$$

where r_n and σ_n^2 are the average and variance of $h_n(r)$, respectively. Physically, Eq. (3) depicts a crystal lattice with accumulated fluctuations with increasing n. This ensures the main characteristics observed in paracrystals. To obtain $g(r)$ via Eqs. (1) and (2), a detailed knowledge of $h_1(r)$ is needed. Once $h_1(r)$ is properly described, the corresponding two-point spatial correlation functions in both real and reciprocal spaces can be constructed. Therefore, $h_1(r)$ can be regarded as a "generating" function for constructing $g(r)$. In previous studies of paracrystal theory in Cartesian coordinates, a Gaussian distribution function with mean L and variance σ^2 is used to define $h_1(r)$. However, it is not mathematically tractable to calculate the two- and three-dimensional correlation functions using Gaussian distribution as a generating function, where the expression of $h_n(r)$ becomes more cumbersome with increasing n values. Because the domain of $h_1(r)$ is always positive, in this study we adopt the following Gamma distribution function as a basis function:

$$h_1(r) = \frac{A}{\Gamma(\alpha)\beta^{\alpha}} r^{\alpha-1} \exp(-r/\beta) = AF(r;\alpha,\beta), \tag{4}$$

where $h_1(r) = 0$ for $r < 0$, Γ is the gamma function, and A is a constant to ensure that $g(\infty) = 1$. α and β are respectively the shape and scale parameters to characterize the Gamma distribution function $F(r;\alpha,\beta)$. It is instructive to point out that in the case of large α values the functional behavior of $F(r;\alpha,\beta) \sim$ Gaussian function and is reduced to the previous paracrystal studies in one-dimensional space. With a proper A, one can show that the mean and variance of $h_1(r)$ in Eq. (4) are proportional to $\alpha\beta$ and $\alpha\beta^2$, respectively. On the basis of

*huangrn@ornl.gov
†chenw@ornl.gov

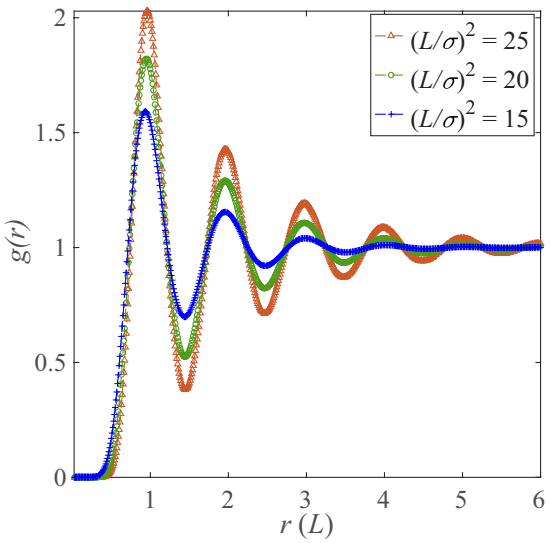

FIG. 1. Theoretical predictions of $g(r)$ by Eq. (6) with parameters: $L = 1$; $1/\sigma^2 = 25$, 20, 15; and $A = 1$. As indicated, the main characteristics of $g(r)$ are determined by the value of $\alpha = L^2/\sigma^2$ and $\beta = \sigma^2/L$, which are related to the ratio of particle fluctuation to lattice size. With increasing L^2/σ^2 or decreasing σ^2/L value, the oscillation behavior gradually becomes discernible, and the variance of each peak accordingly reduces. In addition, $g(r)$ reveals the property of paracrystal whose particle fluctuation is propagated and accumulated throughout particle shells. In long range, $r > 6L$, because of the overlapping fluctuation $g(r)$ converges to unity.

Eqs. (2,4), $h_n(r)$ can be written as

$$h_n(r) = AF(r; n\alpha, \beta). \tag{5}$$

As expected, the functional form of Eq. (5) satisfies the properties of Eq. (3). Therefore, $g(r)$ can be expressed as

$$g(r) = A\sum_{n=1}^{\infty} F(r; n\alpha, \beta). \tag{6}$$

Figure 1 gives several examples of $g(r)$ evaluated according to Eq. (6), with $A = 1$; $\alpha = 25$, 20, 15; and $\beta = \frac{1}{\alpha}$. Using Eq. (6), we proceed to discuss the reciprocal space structures in the following section.

II. TWO-POINT CORRELATION FUNCTIONS IN RECIPROCAL SPACE

In this section, we discuss the two-point correlation functions in reciprocal space, using the phenomenological model constructed in the first part of this paper. In general, the structure factor $S(\mathbf{Q})$ can be evaluated through the Fourier transform of the pair correlation function $g(\mathbf{r}) - 1$ [16],

$$S(\mathbf{Q}) = 1 + \rho\int d\mathbf{r}\exp(-i\mathbf{Q}\cdot\mathbf{r})[g(\mathbf{r}) - 1], \tag{7}$$

where $\mathbf{Q}$ is the momentum transfer of scattered beam particles, r the relative position between two particles, and ρ the number density. In writing Eq. (7), we ignore the contribution of the δ-function term, $(2\pi)^d\rho\delta(\mathbf{Q})$, to the structure factor, where d is the dimensionality of the space. In the presence of radial symmetry, the "radial" part of the structure factor, $S(Q)$, can be directly related to the radial distribution $g(r)$ through cosine, Bessel, and spherical Bessel transforms for one-, two-, and three-dimensional spaces, respectively.

A. One-dimensional structure factor

In the one-dimensional case, Eq. (7) is reduced to

$$S(Q) = 1 + 2\rho\int dr\cos(Qr)[g(r) - 1]. \tag{8}$$

To obtain a compact form of Eq. (8), it is helpful to start with the cosine transform of $h_n(r)$, which is

$$H_n(Q) = 2\int dr\cos(Qr)h_n(r) = 2A\frac{\cos(n\alpha\theta)}{R^n}, \tag{9}$$

where we define the variables $R \equiv (1 + \beta^2Q^2)^{\alpha/2}$ and $\theta \equiv \tan^{-1}(\beta Q)$. Putting Eq. (9) into Eq. (8) we obtain the analytic expression of $S(Q)$ as

$$S(Q) = 1 + 2A\rho\frac{R\cos(\alpha\theta) - 1}{R^2 - 2R\cos(\alpha\theta) + 1}. \tag{10}$$

B. Two-dimensional structure factor

For the isotropic case in two-dimensional space, one shall express Eq. (7) in terms of the Bessel transformation,

$$S(Q) = 1 + 2\pi\rho\int drrJ_0(Qr)[g(r) - 1], \tag{11}$$

where J_0 is the Bessel function of the first kind of order 0. Similarly, the Bessel transformation of $h_n(r)$ is the starting point to calculate Eq. (11). In this case, $H_n(Q)$ is

$$H_n(Q) = 2\pi\int drrJ_0(Qr)h_n(r) = (2\pi\alpha\beta A) \times {}_2F_1\left(\frac{n\alpha+1}{2}, \frac{n\alpha+2}{2}; 1; -\beta^2Q^2\right), \tag{12}$$

where ${}_2F_1$ is the ordinary hypergeometric function. Therefore, the analytical closed form of $S(Q)$ is

$$S(Q) = 1 + B\sum_{n=1}^{\infty} n \times {}_2F_1\left(\frac{n\alpha+1}{2}, \frac{n\alpha+2}{2}; 1; -\beta^2Q^2\right), \tag{13}$$

where $B = 2\pi\alpha\beta A\rho$. It should be noted that Eq. (13), to our best knowledge, does not have a simpler form such as those in Eqs. (10) and (16). Therefore, the application of Eq. (13) might not be useful. Despite this limitation, it is still worthwhile to discuss and explore the physical meaning underlying the behavior of $S(Q)$. The corresponding numerical results of $S(Q)$ are given in Fig. 3.

C. Three-dimensional structure factor

In the three-dimensional case with radial symmetry, Eq. (7) is reduced to the following spherical Bessel transformation:

$$S(Q) = 1 + 4\pi\rho\int drr^2j_0(Qr)[g(r) - 1], \tag{14}$$

where $j_0(x) = \sin(x)/x$ is the spherical Bessel function of the first kind of order 0. The technique to calculate Eq. (14) is

similar to that of one-dimensional case. The first step is to obtain the spherical Bessel transformation of $h_n(r)$. Therefore, we have

$$H_n(Q) = 4\pi \int dr r^2 j_0(Qr) h_n(r)$$
$$= \frac{4\pi A\alpha\beta}{Q} \frac{n}{R^{n+1/\alpha}} \sin[(1+n\alpha)\theta]. \quad (15)$$

Via Eqs. (14) and(15), one can obtain the following analytical form of $S(Q)$:

$$S(Q) = 1 + 2B \frac{R^2 \sin(\phi+\theta) - 2R\sin\theta - \sin(\phi-\theta)}{QR^{1/\alpha-1}[R^2 - 2R\cos(\alpha\theta)+1]^2}, \quad (16)$$

where $\phi = \alpha\theta$. As a guide for the eye, the corresponding results of $S(Q)$ from Eqs. (14) and (16) are given in Fig. 4. In summary, $S(Q)$ of the paracrystal with radial symmetry in one-, two-, and three-dimensional spaces are given in Eqs. (10), (13), and (16). Except for the two-dimensional case, the structure $S(Q)$ can be described by simple analytical expressions.

III. DISCUSSION AND SUMMARY

The structure factor $S(Q)$ of paracrystals with radial symmetry are given in Eqs. (10), (13), and (16). Although a Gamma distribution function is used as a generating function in this work, the one-dimensional results produced by Eq. (10), as shown in Fig. 2, are similar to those in Refs. [1–3], where Gaussian distributions are employed. However, in the two- and three-dimensional cases, the behavior of $S(Q)$, as illustrated in Figs. 3 and 4, is very different from that of Eq. (10) except the first peak around $Q \approx 2\pi/L$. With increasing dimensionality, the upturn in low-Q regime, all the way below $Q \approx 5/L$, becomes more discernible while the high-Q oscillations are strongly suppressed. The origin of the unusual upturn is related to the fact that beyond the first shell the separation between different successive shells is significantly broader than those of typical liquids, such as Leonard-Jones or Yukawa fluids. Namely, the repulsion beyond first shell normally is not as strong as that of first shell to maintain the periodicity of peak position, which is the main characteristic of paracrystals. Therefore, the closer distance between successive shells beyond first nearest-neighbor balances out the upturn and further reflects in the value of the compressibility revealed by $S(0)$. This can be verified by fixing the first peak position and making the other peak positions closer in $g(r)$, as shown in Fig. 5. On the other hand, the frustration of high-Q oscillation could be attributed to the variance of first shell relative to that of other shell in $g(r)$. In paracrystal, the variances of other shells are always n times that of first shell, as indicated in Eq. (3). It can be evidenced by reducing the variance of first shell in $g(r)$ in a factor relative to other shells beyond first peak, as shown in Fig. 6. In summary, we derive general expressions of the spatial correlation function for paracrystals with radial symmetry in one-, two-, and three-dimensional spaces. The validity of analytic scattering functions is confirmed by the direct computation of their Fourier transform. And the physical insight behind the low-Q upturn and high-Q oscillation of scattering functions is discussed and clarified. These results can be further applied to quantify the structural characteristics of paracrystalline materials in real as well as reciprocal spaces via scattering experiments and computer simulations.

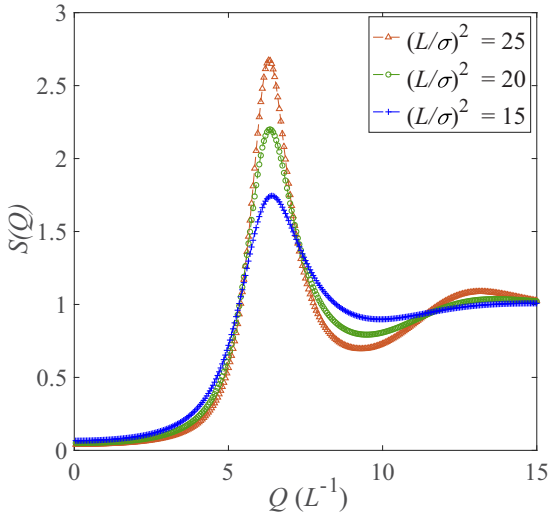

FIG. 2. Theoretical predictions of $S(Q)$ by Eq. (10) and numerical cosine transform of $g(r)$ by Eq. (8) with $\rho = 1$. The other parameters used here are the same as those in Fig. 1. The dash lines and symbols are analytical and numerical results, respectively. The agreement between these curves confirms the validity of Eq. (10). Within the probed Q range, the degree of oscillation becomes more pronounced as L^2/σ^2 increases. For the high-Q regime beyond the second peak, the $S(Q)$ damps to unity rapidly without discernible peaks.

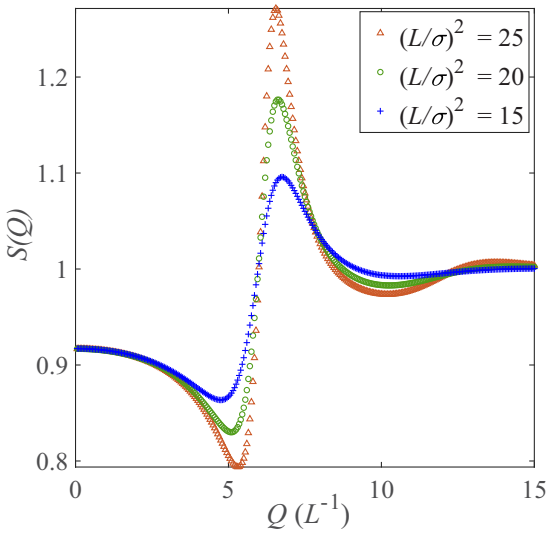

FIG. 3. Numerical computations of $S(Q)$ by Eq. (11) with $\rho = 1/(2\pi)$. All the other parameters used here are the same as those in Fig. 1. Similarly to the one-dimensional case in Fig. 2, within the probed Q range, the first peak becomes more pronounced as L^2/σ^2 increases. Comparing to Fig. 2, the slight upturn of these curves around $Q \approx 5/L$ is observed and beyond $Q \approx 2\pi/L$ the high-Q oscillations are suppressed.

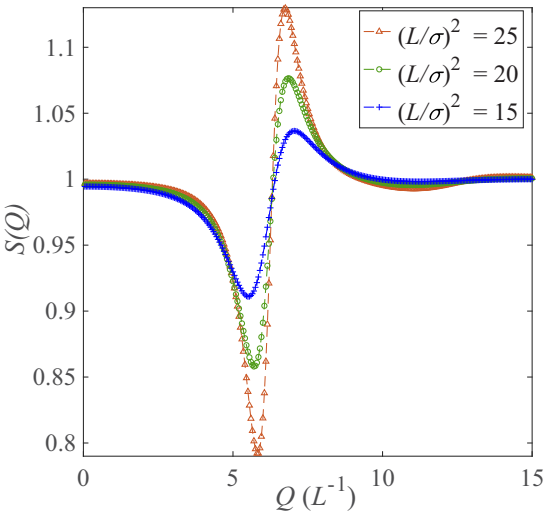

FIG. 4. Theoretical predictions of $S(Q)$ by Eq. (16) and numerical spherical Bessel transform of $g(r)$ by Eq. (14) with $\rho = 1/(4\pi)$. The other parameters used here are the same as those in Fig. 1. The dash lines and symbols are analytical and numerical results, respectively. No noticeable discrepancy between these curves demonstrates the analytical formula of Eq. (16). Similarly, within the probed Q range, the degree of oscillation of first shells gradually becomes more discernible as L^2/σ^2 increases. Compared to the two-dimensional case in Fig. 3 stronger upturn of these curves is observed around $Q \approx 5/L$. Additionally, beyond $Q \approx 2\pi/L$ the high-Q oscillations have nearly vanished.

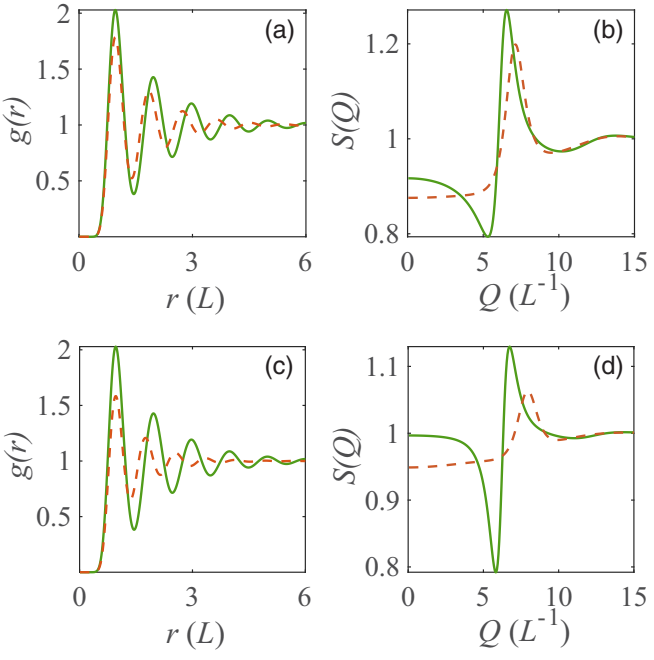

FIG. 5. The origin of the upturn below $Q \approx 5/L$ regime. The two-dimensional case is illustrated in (a) and (b), along with the three-dimensional one in (c) and (d). The green curves have the value of $L^2/\sigma^2 = 25$ for $g(r)$ and $S(Q)$ as those in Figs. 1, 3, and 4. The orange curves are obtained by making the shells closer in the green $g(r)$ of (a) and (c), while keeping that of first shell fixed in the paracrystal with radial symmetry. It is clearly seen that those upturns both in (b) and (d) disappear because of this change.

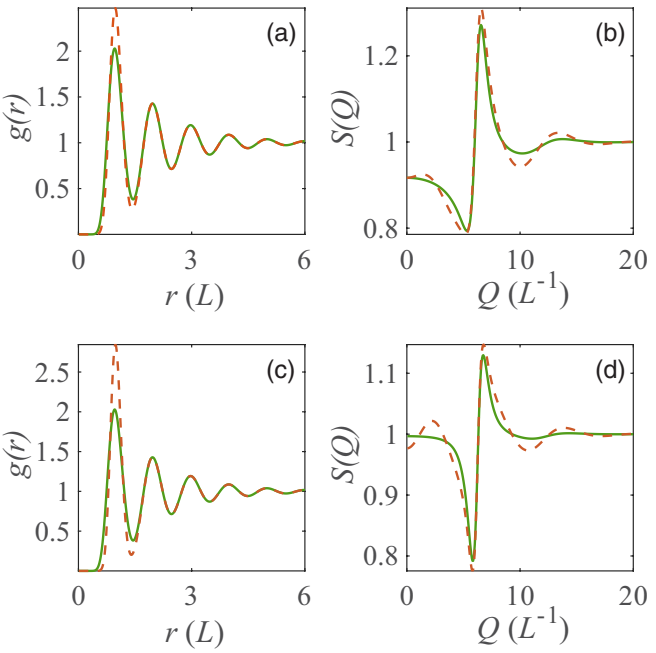

FIG. 6. The origin of vanishing high-Q oscillation in $S(Q)$. Similarly to Fig. 5, the corresponding correlation functions in two- and three-dimensional spaces are illustrated in (a)–(d), respectively. The green $g(r)$ is the same as that of Fig. 5. The orange lines are constructed by reducing the variance of first shell of the green $g(r)$ in (a) and (c), while leaving the other shells unchanged in the paracrystal. It can be seen that in the orange lines of $S(Q)$ in (b) and (d) the high-Q oscillations become discernible.

A natural question that arises from the development of this theoretical spatial correlation function is whether it can be applied to facilitate quantitative structural investigation of materials, in the context of elastic scattering, and obtain additional information which is not available from existing approaches. An area of potential interest is characterization of spherical precipitates in alloys. In the current approaches [17] for small-angle scattering data analysis, the spatial distribution of these second phase particles has been described based on the assumption of hard sphere interaction. Although satisfactory agreement between model fitting and experimental spectra can be obtained from regression analysis, an intrinsic discrepancy between the physical picture embedded in the interacting hard sphere model and the dispersion of these second phase particles is also obvious. Precipitates in alloys are created by mass transport through diffusion [18]. While a strain field is created during the formation process and affects the spatial distribution [19], it is questionable whether hard sphere repulsion can be used to describe the inhomogeneous and complicated interaction among different precipitates. The pair distribution function $g(r)$, which is obtained by Fourier transforming the fitted $S(Q)$ from the solution of Ornstein-Zernike equation with hard sphere interaction [16], is characterized by a sharp peak at $r = D$, where D is the particle diameter. This formation of second phase precipitates in a homogeneous matrix is the result of local solute depletion. As a result, the average distance between a tagged precipitate and its neighbors is considerably larger than

the averaged diameter of precipitates because the physical contact between neighboring precipitates, as indicated by the $g(r)$ of interacting hard spheres, is not energetically favorable [18]. Moreover, the low-Q upturn characterizing the coherent small-angle scattering spectra of precipitating strengthening alloys has been attributed to the effect of grain boundary and polydispersity [17,19–24]. This structural feature can be experimentally assessed by the technique of ultra-small-angle neutron or x-ray scattering. Our calculation suggests that the contribution from multidimensional correlation cannot be disregarded. The deficiency of existing approaches reflects the merits of our phenomenological model for this specific application.

ACKNOWLEDGMENT

This research was supported by the Laboratory Directed Research and Development Program of Oak Ridge National Laboratory, managed by UT-Battelle, LLC, for the U.S. Department of Energy, and performed at SNS, which is DOE Office of Science User Facilities operated by the Oak Ridge National Laboratory. W.-R.C. and G.-R.H. were supported in part by the USANS at SNS. Y.W. acknowledges support by the U.S. Department of Energy (DOE), Office of Science, Office of Basic Energy Sciences, Early Career Research Program Award KC0402010, under Contract No. DE-AC05-00OR22725. G.-R.H. acknowledges the support from Ministry of Science and Technology in Taiwan under Grant No. MOST 108-2917-I-564-013.

This work has been partially supported by UT-Battelle, LLC under Contract No. DE-AC05-00OR22725 with the U.S. Department of Energy. The United States Government retains and the publisher, by accepting the article for publication, acknowledges that the United States Government retains a non-exclusive, paid-up, irrevocable, worldwide license to publish or reproduce the published form of this manuscript, or allow others to do so, for United States Government purposes. The Department of Energy will provide public access to these results of federally sponsored research in accordance with the DOE Public Access Plan [25].

[1] R. Hosemann, Crystallinity in high polymers, especially fibres, Polymer **3**, 349 (1962).

[2] R. Bonart, R. Hosemann, and R. L. Mccullough, The influence of particle size and distortions upon the x-ray diffraction patterns of polymers, Polymer **4**, 199 (1963).

[3] A. Guinier, *X-ray Diffraction in Crystals, Imperfect Crystals, and Amorphous Bodies* (W. H. Freeman & Company, San Francisco, CA, 1963).

[4] W. Ruland, Crystallinity and disorder parameters in nylon 6 and nylon 7, Polymer **5**, 89 (1964).

[5] F. Briki, B. Busson, and J. Doucet, Organization of microfibrils in keratin fibers studied by s-ray scattering modelling using the paracrystal concept, Biochim. Biophys. Acta **1429**, 57 (1998).

[6] B. Steffen and R. Hosemann, Paracrystalline microdomains in monatomic liquids. I. Radial density functions of liquid lead at 350, 450, and 550 °C; and II. Three-dimensional structure of microdomains in liquid lead, Phys. Rev. B **13**, 3227 (1976).

[7] H. Matsuoka, H. Tanaka, T. Hashimoto, and N. Ise, Elastic scattering from cubic lattice systems with paracrystalline distortion, Phys. Rev. B **36**, 1754 (1987).

[8] R. Hosemann, Crystalline and paracrystalline order in high polymers, J. Appl. Phys. **34**, 25 (1963).

[9] R. Hosemann, M. P. Hentschel, F. J. Balta-Calleja, and G. S. Y. Yeh, Generalisation of P. P. Ewald's intensity function for microparacrystals in colloids and their superstructures, J. Phys. C: Solid State Phys. **16**, 4959 (1983).

[10] R. Hosemann, A. M. Hindeleh, and R. Brückner, Paracrystalline lattice structure of silica glass, α- and β-crystobalite, Phys. Status Solidi (a) **126**, 313 (1991).

[11] R. Hosemann and A. M. Hindeleh, Structure of crystalline and paracrystalline condensed matter, J. Macromol. Sci. B **34**, 327 (1995).

[12] M. M. J. Treacy, J. M. Gibson, and P. J. Keblinski, Paracrystallites found in evaporated amorphous tetrahedral semiconductors, J. Non-Cryst. **231**, 99 (1998).

[13] A. Marx, J. Pless, E. M. Mandelkow, and E. Mandelkow, On the rigidity of the cytoskeleton: Are MAPs crosslinkers or spacers of microtubes? Cell. Mol. Biol. **46**, 949 (2000).

[14] S. M. Nakhmanson, P. M. Voyles, N. Mousseau, G. T. Barkema, and D. A. Drabold, Realistic models of paracrystalline silicon, Phys. Rev. B **63**, 235207 (2001).

[15] K. Jurkiewicz, M. Kamiński, W. Glajcar, N. Woźnica, F. Julienne, P. Bartczak, J. Polański, J. Lelatko, M. Zubko, and A. Burian, Paracrystalline structure of gold, silver, palladium, and platinum nanoparticles, J. Appl. Cryst. **51**, 411 (2018).

[16] J. P. Hansen and I. R. McDonald, *Theory of Simple Liquids* (Academic Press, London, 2006).

[17] For example, see J. S. Pedersen, Small-angle scattering from precipitates: Analysis by use of a polydisperse hard-sphere model, Phys. Rev. B **47**, 657 (1993).

[18] D. A. Porter, K. E. Easterling, and M. Sherif, *Phase Transformations in Metals and Alloys, 3rd ed.* (CRC Press, Boca Raton, FL, 2009).

[19] J. D. Eshelby, The determination of the elastic field of an ellipsoidal inclusion, and related problems, Proc. R. Soc. Lond. Ser. A **241**, 376 (1957).

[20] A. D. Sequeira, H. A. Calderon, G. Kostorz, and J. S. Pedersen, Bimodal size distributions of γ' precipitates in Ni-Al-Mo—I. Small-angle neutron scattering, Acta Metall. Mater. **43**, 3427 (1995).

[21] J. S. Pedersen, A. Horsewell, and M. Eldrup, A small-angle neutron scattering and transmission electron microscopy study of krypton precipitates in cooper, J. Phys.: Condens. Matter **8**, 8431 (1996).

[22] C.-S. Tsao, T.-L. Lin, and M.-S. Yu, δ' precipitation in Al-9.7at%Li alloy using small-angle X-ray scattering, J. Alloys Compd. **289**, 81 (1999).

[23] G. A. Zickler, B. Tian, C. Lind, and O. Pairs, Separation of scattering contributions from carbides and γ' precipitates in Nimonic 80a by combining small-angle X-ray and neutron scattering, J. Appl. Cryst. **36**, 484 (2003).

[24] S. A. Briggs, P. D. Edmondson, K. C. Littrell, Y. Yamamoto, R. H. Howard, C. R. Daily, K. A. Terrani, K. Sridharan, and K. G. Field, A combined APT and SANS investigation of α' phase precipitation in neutron-irradiated model FeCrAl alloys, Acta Mater. **129**, 217 (2017).

[25] http://energy.gov/downloads/doe-public-access-plan.